Research Article | Vol. 10, No. 12 / 1 December 2019 / Biomedical Optics Express 6172
Biomedical Optics EXPRESS

Gold nanoisland substrates for SERS characterization of cultured cells

ADRIANNA MILEWSKA,[1,2,3] VESNA ZIVANOVIC,[4] VIRGINIA MERK,[4] UNNAR B. ARNALDS,[5] ÓLAFUR E. SIGURJÓNSSON,[2,6] JANINA KNEIPP,[4] AND KRISTJAN LEOSSON[1,5,*]

[1] *Innovation Center Iceland, Árleynir 2–8, 112 Reykjavík, Iceland*
[2] *The Blood Bank, Landspitali University Hospital, Snorrabraut 60, 105 Reykjavík, Iceland*
[3] *University of Iceland, School of Engineering and Natural Sciences, Sæmundargötu 2, 101 Reykjavík, Iceland*
[4] *Humboldt University, Brook-Taylor-Str. 2, 12489, Berlin, Germany*
[5] *Science Institute, University of Iceland, Dunhaga 3, 107 Reykjavík, Iceland*
[6] *Reykjavik University, School of Science and Engineering, Menntavegur 1, 101 Reykjavík, Iceland*
[*] *kristjan.leosson@nmi.is*

Abstract: We demonstrate a simple approach for fabricating cell-compatible SERS substrates, using repeated gold deposition and thermal annealing. The substrates exhibit SERS enhancement up to six orders of magnitude and high uniformity. We have carried out Raman imaging of fixed mesenchymal stromal cells cultured directly on the substrates. Results of viability assays confirm that the substrates are highly biocompatible and Raman imaging confirms that cell attachment to the substrates is sufficient to realize significant SERS enhancement of cellular components. Using the SERS substrates as an *in vitro* sensing platform allowed us to identify multiple characteristic molecular fingerprints of the cells, providing a promising avenue towards non-invasive chemical characterization of biological samples.

1. Introduction

Raman scattering spectroscopy has emerged as a powerful tool in biological studies [1–3], as a label-free and potentially non-invasive imaging method providing chemical specificity. Raman scattering refers to the physical phenomenon in which photons incident on a sample are inelastically scattered, losing or gaining energy corresponding to vibrational energy quanta of molecules in the sample under investigation [3,4]. Raman scattering is inherently weak compared to elastic (Rayleigh) scattering, with only around 1 in 10^8 photons being inelastically scattered [2,3]. This low scattering efficiency can be overcome by positioning the scattering molecules in close proximity to metallic nanostructures, where excitation of surface plasmons results in locally enhanced electric fields at the metal surface. This phenomenon is known as surface-enhanced Raman scattering (SERS). Since its discovery [5–7], a wide variety of metal nanostructures have been used to realize SERS. As an example, SERS can be obtained at the surface of colloidal nanoparticles or clusters of nanoparticles mixed into the sample solution, or by placing the sample on surfaces nanostructured by, e.g., electrochemical etching, dispersion of particles, or using high-resolution patterning techniques [8,9]. In particular gold and silver are among the preferred choices for SERS applications due to their suitable dielectric properties at optical frequencies.

For studying biological cells, a common approach for obtaining SERS enhancement involves the addition of colloidal nanoprobes of gold or silver [10–13]. This approach poses some limitations, such as irreversible uptake (which is technically invasive), uncontrollable localization and the tendency of particles to aggregate with time [13]. Functionalization of SERS probes with specific peptides [14] is one way to overcome this obstacle. However, the conjugated probes

#378646 https://doi.org/10.1364/BOE.10.006172
Journal © 2019 Received 20 Sep 2019; revised 1 Nov 2019; accepted 3 Nov 2019; published 8 Nov 2019

Biomedical Optics EXPRESS

might be the source of a background in SERS signal, which may interfere with the signals coming from the cells [15].

An alternative option is studying cells grown on SERS-active surfaces [16–18]. Although this limits the volume of study to the parts of the cell adjacent to the substrate, it provides the potential for non-invasive *in vitro* study of cells. Over the last few decades, substantial efforts have been devoted to developing nanostructured SERS surfaces in order to provide the largest signal enhancement, mainly for identifying particular molecules in solution. These include island films [19–21], plasmonic nanowires [22], nanostars [23,24], nanobundles [25], nanocubes and nanoblocks [26], nanofingers on nanowires [27] and nanoantennas [28]. Using such surfaces, enhancement of scattering efficiency ranging from 10^6 to 10^{12} has been realized, compared to the corresponding Raman signals obtained in the absence of metallic nanostructures. However, production of nanostructures with high SERS efficiency can be complex, time-consuming and costly. Moreover, the largest enhancements are typically only realized in very small volumes, compared to the overall sample volume [29].

In order to facilitate SERS-imaging of biological cells on nanostructured surfaces, substrates with sufficiently high enhancement and homogeneous distribution of so called hot-spots are needed, while also making sure that the substrate is suitable for cell growth. Numerous procedures have been explored to fabricate substrates with a dense and uniform distribution of hot-spots, including nanopatterns produced by electron-beam lithography [30] or metal deposition on high-aspect-ratio structures such as leaning nanopillars [31]. Such substrates are typically difficult to fabricate and/or unsuitable for cell growth and subsequent microscope imaging. For cell culturing experiments, ideal SERS substrates and information about their biocompatibility are still in short supply [18,32]. Such substrates should exhibit uniform and repeatable enhancement across large areas, they should be reasonably flat for improved cell attachment and imaging and allow for imaging through the SERS-active layer using an inverted microscope. Preferably, they should also be easily fabricated at low cost.

Here, we use a simple method for fabricating cell-compatible SERS substrates on glass cover slips by repeated gold deposition and thermal annealing. In order to demonstrate the applicability of such substrates for culturing and subsequent SERS imaging of cells, we have used these substrates to study bone marrow-derived mesenchymal stromal cells (BM-MSCs). BM-MSCs can be described as multipotent progenitors that are plastic-adherent under standard cell culture conditions *in vitro* and are able to undergo osteogenic, adipogenic and chondrogenic differentiation [33,34]. Their clinical potential has been evaluated for various types of tissue injuries and immune diseases [35], angiogenesis [36], but also cancer invasion and metastasis [37]. Characterization of mesenchymal stromal cells in order to understand the processes of cellular propagation and their interaction with external environment has received increasing attention. To date, available tools for studying cells include biological assays, chromatography, western blot analysis, quantitative polymerase chain reaction (qPCR) and immunofluorescence staining [38,39]. However, these assessment processes have major disadvantages, such as being time-consuming and invasive, involving specific sample preparation and use of labels, but more importantly they require termination of the cell culture in order to perform the analysis. Therefore, a critical need has arisen to develop a method that will enable sensitive characterization of chemical properties of the cells, while leaving them undisturbed on the substrate. In the work presented here, we describe SERS imaging of such cells cultured on the gold nanoisland substrates.

2. Materials and methods

2.1. Fabrication and characterization of SERS substrates

The fabrication of gold nanoislands on 18×18 mm cover glass (Marienfeld, Germany) supports was achieved by repeated metal deposition and post-deposition annealing, similar to that reported

Biomedical Optics EXPRESS

in Refs. [20,21]. An electron-beam evaporator (Polyteknik Cryofox Explorer 600 LT) was evacuated to a base pressure of 6.0×10^{-5} mbar. Thin layers of 99.95% gold with thickness below the percolation threshold were deposited (corresponding to a mass-equivalent thickness of approximately 4 nm using a 0.6 Å/s deposition rate), thereby producing self-organized gold nanoparticle (AuNP) islands. The as-coated cover glasses were annealed immediately after deposition on a hot plate at 500°C for 5 minutes, causing aggregation of smaller AuNPs into larger particles through surface diffusion. Subsequently, similar gold deposition and post-deposition annealing steps were repeated up to a total of three times to eventually obtain a nano-patterned gold film with a wide distribution of particle sizes. The process is shown schematically in Fig. 1. After the last annealing step, the substrates were used directly for cell culturing experiments, as described below.

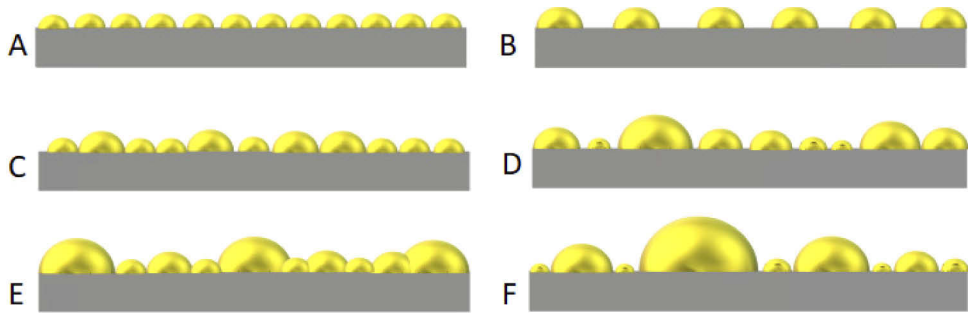

Fig. 1. Schematic illustrations of the fabrication process involving repeated gold deposition (A, C, E) and subsequent post-deposition thermal annealing (B, D, F) resulting in nanoparticle aggregation.

The gold film structure was characterized by a Zeiss Supra-25 scanning electron microscope (SEM) using an in-lens detector. The planar morphology of AuNPs, i.e. surface coverage, mean diameter of gold nanoparticles and average distance between them, were obtained from the SEM images using Image-J software (NIH, Bethesda, MD, USA). In addition, the surface topography was evaluated using a XE-100 atomic force microscope (Park Systems) with a scan size of 1–2 μm and a scan rate of 0.15 Hz in non-contact mode, using conventional silicon cantilevers.

2.2. Preparation of cell suspension solution

Mesenchymal stromal cells (MSCs) derived from the bone marrow were purchased from Lonza (Lonza, Walkersville, MD, USA) and stored at −196°C in liquid nitrogen prior to experimentation. The cells were thawed in a 37°C water bath and transferred into a pre-heated DMEM/F12 + glutamax medium (Gibco, Grand Island, NY, USA) containing 1% penicillin/streptomycin (Gibco, Grand Island, NY, USA), 2 IU/ml heparin (Leo Pharma A/S, Ballerup, Denmark) supplemented with 10% human platelet lysates (hPL; Platome, Reykjavik, Iceland), referred to as "expansion medium" and centrifuged at 609×g for 5 minutes (1750rpm) to minimize the effects of DMSO (IDT Biologika GmbH, Steinbach, Germany) preservation. DMSO is used during the storage of MSCs in liquid nitrogen to prevent cell rupture. The supernatant was discarded, and the cells were resuspended in 1 ml of preheated expansion medium before being seeded into a tissue culture flask at a density of 6000 cells/cm^2. The Nunc EasYFlask 75 cm^2 (T75) tissue culture flask (Thermo Fischer Scientific Nunc A/S, Roskilde, Denmark) was placed in a 95% humidified incubator with 5% CO_2 and temperature at 37°C. The cell culture medium was replaced every 2–3 days. At 80–90% confluence, cells were gently washed with PBS pH 7.4 (Gibco, Grand Island, NY, USA) and detached from the surface in 0.25% Trypsin-EDTA (Gibco, Grand Island, NY, USA) for 5 minutes. An equal amount of preheated expansion medium was

Biomedical Optics EXPRESS

added to neutralize the trypsin before the cells were centrifuged at 609×g for 5 minutes (1750rpm). After centrifugation, the supernatant was discarded, and the cell pellet was re-suspended in 1 ml of the expansion medium prior to cell counting. The cells were diluted by mixing 20 µl re-suspended cell solution, 30 µl PBS and 50 µl 0.4% Trypan Blue stain (Gibco, Grand Island, NY, USA). The cell solution was transferred onto a hemocytometer (BRAND GmbH & Co. KG, Wertheim, Germany) covered by a glass cover slip and counted at 50× magnification using a Leica DM IRB inverted microscope (Leica Microsystems, Wetzlar, Germany). Viable cells were identified by their lack of Trypan Blue uptake. Cell passaging was completed by seeding cells on the SERS substrates.

2.3. Cell culture on SERS substrates

SERS substrates, along with glass controls, were placed in 2-well chamber slides (NuncLab-Tek Chamber Slide System, Thermo Fischer Scientific Nunc A/S, Roskilde, Denmark) and exposed to a high dose of UV light for 40 minutes to ensure proper sterilization. 5.500 cells/cm^2 were seeded onto the SERS substrates and transferred to a shaking incubator at 37°C for 3–4 minutes to ensure proper attachment of the cells to the substrates. Subsequently, 1 ml of expansion medium was added to each well and maintained at 37°C in a 95% humidified atmosphere with 5% CO_2. The complete cell culture medium was replaced every two to three days and the cell culture was terminated on day seven. The cell culture medium was discarded, the cells were washed three times with PBS and fixed for subsequent SERS measurements and immunofluorescence staining as described below.

2.4. PrestoBlue viability assay

Cell proliferation was assessed by the PrestoBlue (PB) method [40]. Living cells reduce the PrestoBlue reagent (Resazurin), and the end product (Resofurin) can be measured with a spectrophotometer. The amount of converted reagent is proportional to the number of metabolically active cells. Briefly, MSCs on the SERS substrates and glass controls were incubated at 37°C for 2 hours in expansion medium spiked with PrestoBlue reagent (Thermo Fisher Scientific, Frederick, MD, USA) in a 9:1 ratio. After a visually determined color change, 100 µl of medium from each well was transferred to a 96-well plate in triplicate and the absorbance was measured in the wavelength range 570–600 nm. The assay was performed on days 1, 3 and 7.

2.5. LDH cytotoxicity assay

Lactate dehydrogenase (LDH) is a cytoplasmic oxidoreductase that is released into the culture supernatant when the plasma membrane is damaged [41]. The degree of potential cellular injury thus can be monitored by measuring the amount of LDH released by the cells. In this study, LDH level in the culture medium of MSCs grown on SERS substrates and glass controls was assessed on days 1, 3 and 7 using a Pierce LDH Cytotoxicity Assay (Thermo Fisher Scientific, Rockford, IL 61105, USA) following the manufacturer's protocol.

2.6. Immunofluorescence microscopy

Prior to immunofluorescence staining, cells on SERS substrates were fixed with 4% paraformaldehyde for 20 minutes at room temperature and subsequently blocked with 1% bovine serum albumin - BSA (Thermo Fisher Scientific, Rockford, IL 61105, USA) in PBS for 30 minutes. Samples were incubated with primary antibody Anti-Vinculin (FAK100, Merck KGaA, Darmstadt, Germany) diluted 1:500 in blocking solution for 1 h at room temperature. Following incubation with primary antibody, samples were incubated (1 h at room temperature) with secondary antibody Goat Anti-Mouse IgG, H + L FITC (Abcam plc, Cambridge, CB2 0AX, UK) and TRITC-conjugated Phalloidin (FAK100, Merck KGaA, Darmstadt, Germany) both diluted 1:1000 in PBS. Subsequently, 4'6-Diamidino-2-phenylindole – DAPI (FAK100, Merck KGaA,

Biomedical Optics EXPRESS

Darmstadt, Germany) diluted 1:1000 in PBS was applied for 5 minutes. SERS substrates were then washed with buffer solution and mounted on glass slides using SlowFade Gold Antifade Mountant with DAPI (Thermo Fisher Scientific, Rockford, IL 61105, USA). Between all the above-mentioned steps in the sample processing, the SERS substrates with the cells were washed with 0.1% Triton X-100 (Sigma-Aldrich, St. Louis, MO, USA) in PBS washing buffer. Control samples on conventional culture slides were stained in the same manner. Immunofluorescence was visualized and captured using an Olympus FV1200 (Olympus, Tokyo, Japan) confocal laser scanning microscope. Image panels were constructed using Image-J software (NIH, Bethesda, MD, USA).

2.7. Raman experiments and estimation of EFs

Normal Raman and SERS spectra were recorded over a spectral range of 300 cm^{-1} to 1900 cm^{-1} using a single-stage spectrograph (Horiba, Munich, Germany) with a CCD detector and a 60× water-immersion objective (Olympus, Hamburg, Germany). For excitation, a diode laser (Toptica, Munich, Germany) operating at 785 nm was used (1 µm laser spot size). In order to experimentally determine the SERS enhancement factor (EF) of the substrates, Raman signals from crystal violet (CV) were collected, with and without SERS enhancement. The excitation intensity on the sample was 2.0×10^5 $W{\cdot}cm^{-2}$ and an acquisition time of 1 s per spectrum was used. The CV concentration was $1{\cdot}10^{-4}$ M in the SERS experiments while in the normal Raman experiments the CV concentration was $1{\cdot}10^{-2}$ M. Both were performed in aqueous solution. Typical spectra in the SERS experiment on cells were collected using intensity on the sample of 2.0×10^5 $W{\cdot}cm^{-2}$, with a raster size of 2 µm and an acquisition time of 3 s per spectrum. All spectra were frequency-calibrated using a spectrum of a toluene-acetonitrile mixture (1:1). Chemical maps were prepared using CytoSpec 2.00.06 software (CytoSpec, Inc.).

SERS enhancement factors were estimated by comparing intensities in the normal Raman spectrum (I_{RS}) and in the SERS spectrum (I_{SERS}) for the band at 1618 cm^{-1} of crystal violet (see Fig. 4(A) below), taking into account the number of molecules in the focus volume (N_{RS}) versus the number of molecules on the nanoparticle surface (N_{SERS}), assuming a surface area per CV molecule of 4 nm^2 [42].

$$EF = \frac{I_{SERS} N_{RS}}{I_{RS} N_{SERS}}$$

3. Properties of the SERS substrates

3.1. Properties of the nanostructured surfaces

SEM images of the development of the gold film structure during the repeated steps of deposition and annealing are shown in Fig. 2(A). In the first step, the initial gold deposition gives rise to a discontinuous metal film, consisting of very small (<5 nm) isolated islands. After thermal annealing, the small islands merge into nanoparticles with an average diameter of about ~20 nm. The size distribution of AuNPs is shown by the histograms in Fig. 2(B) (shown as the diameter of circular particles having equivalent area). Repeating the gold deposition and annealing steps resulted in a bimodal size distribution of larger (average diameter of ~37 nm) and smaller (average diameter ~7 nm) particles, while simultaneously decreasing the average minimum distance between adjacent particles and increasing the surface coverage from 40% after Step 1 to about 55% after Step 3. It is well known that the small gaps between neighboring nanoparticles are the regions where the highest plasmonic enhancement occurs [11,43]. Those nanogaps are often referred as “hot-spots”. It was noted before [21], however, that the size distribution of islands is also an important factor in determining the overall SERS enhancement.

The surface topography after each deposition and annealing step is shown in Fig. 3(C). After each cycle the mean particle height was increasing (9 nm, 18 nm and 24 nm, respectively), correlating well with the total deposition thickness and measured surface coverage at each step.

Biomedical Optics EXPRESS

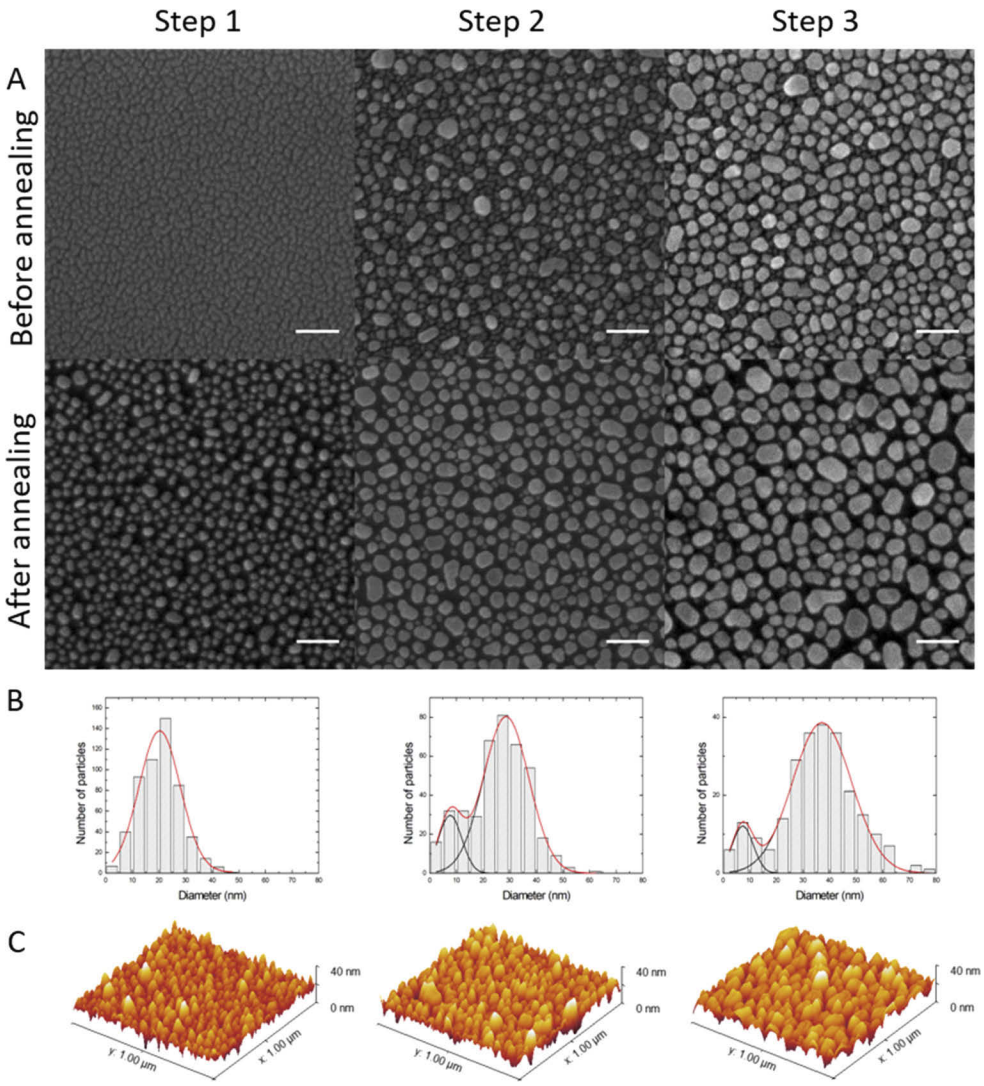

Fig. 2. A) Scanning electron micrographs of SERS substrates at different stages of fabrication. Upper images correspond to 1st, 2nd and 3rd gold deposition and lower images correspond to 1st, 2nd and 3rd thermal annealing. All scale bars represent 100 nm. B) Particle size distributions corresponding to each step of sample fabrication after annealing. C) AFM images corresponding to sequential steps of deposition and post-deposition annealing (step 1, 2 and 3).

Beyond Step 3, the film eventually reaches the percolation threshold, decreasing the number and intensity of hotspots on the film surface.

Prior to annealing, the deposited structures exhibit transmission and reflection spectra similar to gold films below the percolation limit deposited on an untreated glass surface [44]. After annealing, the spectra are modified and a clear absorption maximum around 550 nm is observed (absorption was estimated as 1-T(λ)-R(λ), ignoring potential scattering out of the detection path which we take to be negligible for this sub-diffractive structure). With increasing deposition thickness, the disordered particle array gives increasing additional broadband absorption, extending from the fundamental resonance to beyond 900 nm wavelength. Similar behavior is seen for multiple

Biomedical Optics EXPRESS

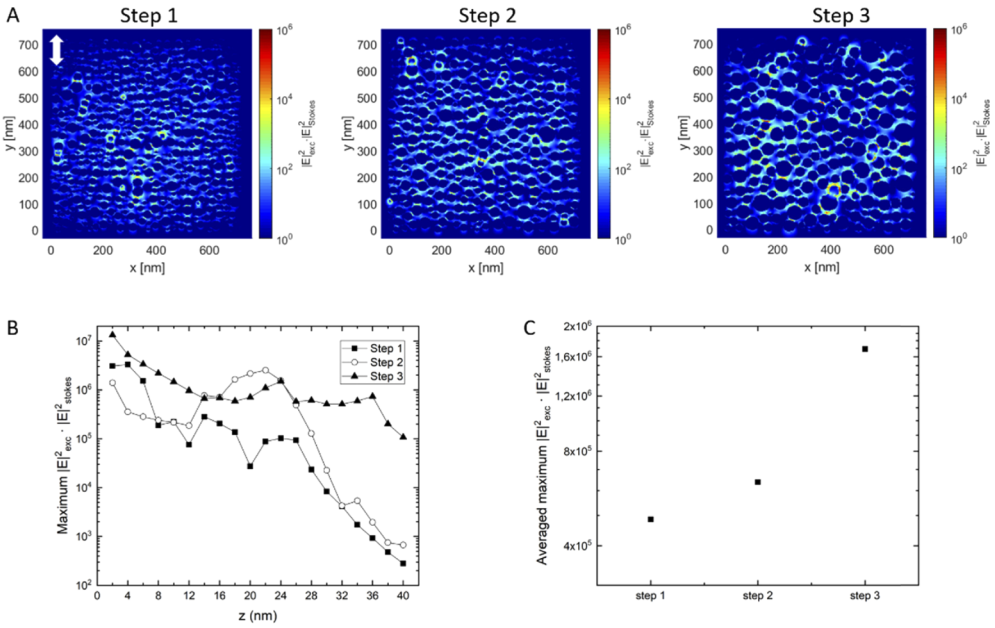

Fig. 3. A) FDTD simulations showing the product of field intensities at an excitation wavelength of 785 nm and a Raman scattered wavelength of 830 nm ($|E|^2_{exc} \cdot |E|^2_{Stokes}$), which relates to the SERS enhancement in the experiment. The calculations were performed for structures modelled according to the gold particle geometry following steps 1, 2 and 3 of substrate fabrication (Fig. 2A). The direction of polarization of the incident light is indicated with the white arrow. B) Maximum product of field intensities at excitation wavelength 785 nm and Stokes wavelength 830 nm for different heights above the glass surface. C) Maximum field enhancement factor obtained by FDTD simulations for sequential fabrication steps, averaged over the simulated range of heights and Stokes wavelengths.

deposition and annealing cycles in templated gold nanostructures where it correlated with observations of broadband (up to ≈1000-fold) field intensity enhancement in the 600–1000 nm wavelength range [45].

3.2. *Distribution of the local field intensity from FDTD simulations*

In order to get an understanding of the electromagnetic field distribution at the surface of the SERS substrates, we carried out 3D finite-difference time domain (FDTD) simulations, using commercially available software (FDTD Solutions, Lumerical Inc., Vancouver, BC, USA). Actual SEM images were used to build realistic geometrical models for the irregular AuNPs films, consisting of spherically capped cylindrical particles with radii and cylinder heights corresponding to the equivalent particle radius determined from SEM measurements (Fig. 2(A)). The simulation mesh size around the gold layer was 2 nm. The frequency-dependent dielectric function of Au was taken from Ref. [46] and the refractive index of the surrounding dielectric was set to 1.33 to represent the aqueous environment in our SERS measurements.

Results of FDTD simulations for the three steps of sample fabrication are shown in Fig. 3(A), corresponding to the particle size distributions shown in Fig. 2(B). Representative maps of the product of the electric field intensities at the excitation wavelength (785 nm) and the Raman-scattered wavelength at 830 nm are shown, corresponding to the band at 1618 cm^{-1}, used to estimate the electromagnetic contribution to the SERS EF [47]. The field maps are plotted for a distance of 2 nm from the glass surface. Importantly for SERS studies of cells grown on the

Biomedical Optics EXPRESS

nanostructured surfaces, however, Fig. 3(B) illustrates how repeated deposition and annealing results in higher maximum enhancement values that are also substantially more extended from the glass surface. FDTD simulations indicate that the field enhancement factor is consistent across the typical range of emission wavelengths used here, typically varying within approximately a factor of 3–4 for Stokes shifts up to 2200 cm^{-1}. The simulated maximum field enhancement factor (averaged for heights 2–40 nm and Stokes shifts 0–2200 cm^{-1}) corresponding to each deposition and annealing step is shown in Fig. 3(C).

3.3. SERS enhancement factor from experiments

In order to provide experimental proof of the influence of average local field enhancement on our fabricated SERS substrates, experiments using CV as analyte were performed (Fig. 4(A)), as described above (although we do emphasize that local field enhancement is not the only mechanism underlying observed SERS enhancements [48,49]). The experimentally determined EF values for subsequent fabrication steps are shown in Fig. 4(B). In accordance with electromagnetic field simulations, the maximum SERS enhancement factor was obtained after step 3 of substrate fabrication. In this case, 36 measurements at different points on the SERS substrate (inset of Fig. 4(B)) gave an average EF value of $9{\cdot}10^5$, exhibiting also a better uniformity across the substrate than for the preceding fabrication steps, with a relative standard deviation of 7%. After step 1, the average measured enhancement factor was $1{\cdot}10^4$ with relative standard deviation of 24%, while for step 2 it was $1{\cdot}10^5$ with a standard deviation of 33%.

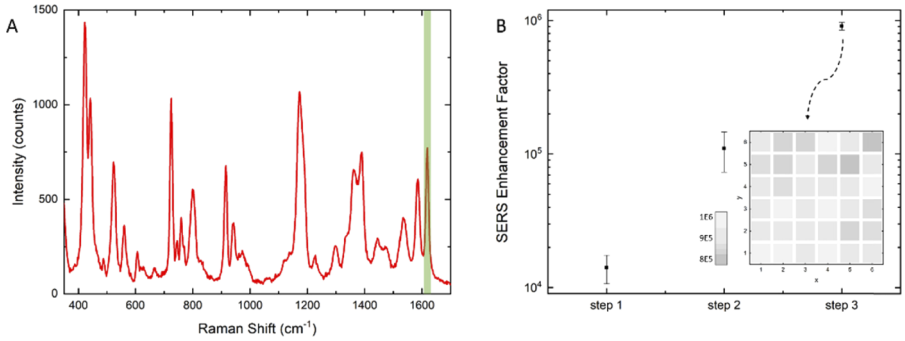

Fig. 4. A) Representative single SERS spectrum of crystal violet (c = 10^{-4} M). The signal at 1618 cm^{-1} (marked in green) was used to estimate the enhancement factor (excitation: 785 nm, intensity: 2.0×10^5 W·cm^{-2}, acquisition time: 1 s). B) Experimentally determined SERS enhancement factor for each step of substrate fabrication. Inset: Schematic distribution of enhancement factors at positions (x,y) on a substrate after three deposition and annealing steps. Data points are separated by 10 µm in x and y and the diameter of the probed spot was 1 µm (not to scale in the schematic).

4. Analysis of BM-MSC cultures on SERS substrates

4.1. Qualitative cell viability assays

Cell proliferation on SERS substrates (after fabrication step 3) was determined with PrestoBlue assay. Three identically prepared substrates were tested, in addition to three glass controls. Cell expansion was increasing with time on all substrates, with the greatest extent on day 7 (Fig. 5(A)). Cell proliferation remained low until day 3, on day 7 the level was notably higher. No significant differences were observed between the three SERS substrates at any point in time during expansion. Cell proliferation was only slightly lower on the SERS substrates than on the glass controls. Lactate dehydrogenase (LDH) release was evaluated as a marker for cytotoxicity.

Biomedical Optics EXPRESS

The results demonstrated that none of the substrates tested had cytotoxic effects to the cells after days 1, 3 and 7 (Fig. 5(B)). LDH release was low (cytotoxic percentage did not exceed 25%) and decreased with time. No significant differences were observed between the SERS substrates on one hand, and glass controls on the other hand. Therefore, both PrestoBlue and LDH assays indicated that the SERS substrates do not disturb cell proliferation or induce cell death.

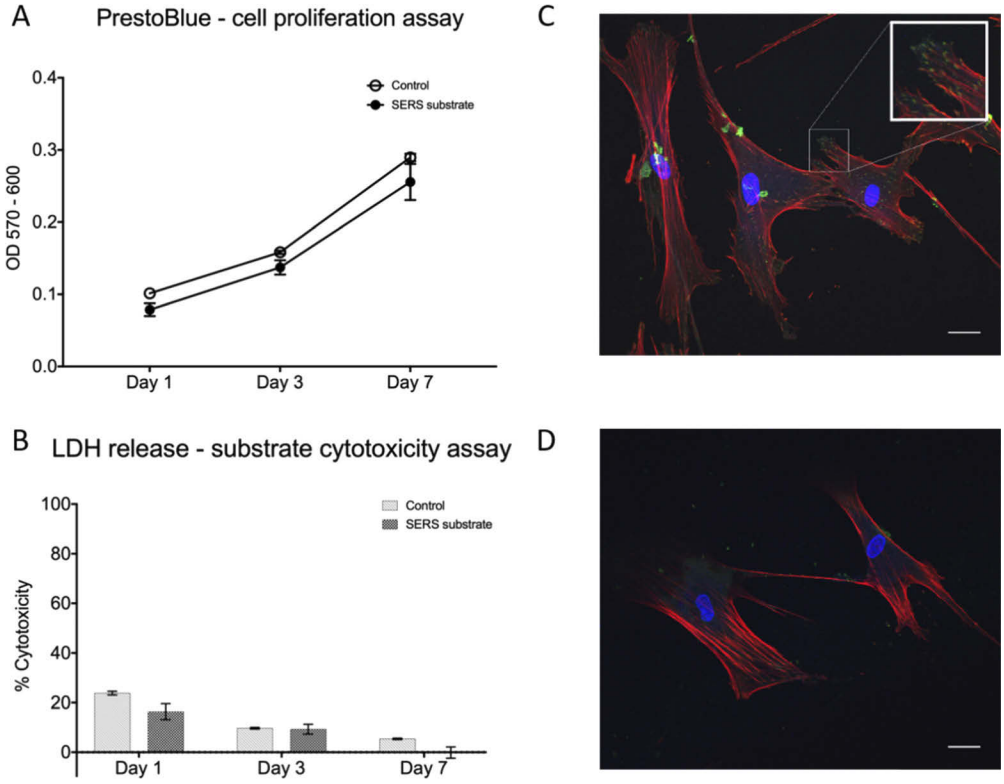

Fig. 5. A) Results for PrestoBlue cell proliferation assay for BM-MSCs cultured on glass controls and on SERS substrates (n = 3), error bars represent the standard deviation. B) Results for LDH cell cytotoxicity assay for BM-MSCs cultured on glass controls and SERS substrates (n = 3), error bars represent the standard deviation. C) Representative confocal image of focal adhesion plaques (green), actin cytoskeleton (red) and nuclei of mesenchymal stromal cells (blue) grown on a SERS substrate and D) on a conventional culture slide as control. Scale bars: 20 µm.

4.2. Mesenchymal stromal cells attach to the SERS substrates

In order to investigate the interaction between the mesenchymal stromal cells and the SERS substrates, immunofluorescence staining was performed, followed by imaging with a confocal laser scanning microscope (Fig. 5(C)). Within the first few days of the cell culture, the cell bodies attached to the SERS substrate. Over time, the cell adhesion became stronger and cells started flattening and spreading out over the substrates. Actin filaments, detected with TRITC-conjugated Phalloidin, were organized in a predominantly parallel manner (Fig. 5(C)). Mouse anti-Vinculin monoclonal antibody and FITC-conjugated secondary antibody revealed a clear evidence of focal adhesion plaques (Fig. 5(C) magnified image) between cells and the underlying substrate. A fluorescent stain 4'6-Diamidino-2-phenylindole (DAPI), which binds strongly to A-T rich regions in DNA, exposed the cellular nuclei (blue). Compared to the single cells grown on a conventional

Biomedical Optics EXPRESS

culture slide (Fig. 5(D)), cells on the SERS substrates tended to grow in a higher density with less space between them.

5. Results of SERS analysis of BM-MSCs

5.1. Confirmation of SERS enhancement in Raman spectra from fixed cells

The enhancement of Raman scattering was observed also after culturing cells on the SERS substrates, as was confirmed by Raman imaging of the cells. Before the SERS measurements, the BM-MSC cells were cultured on the SERS substrates for seven days, fixed using 4% paraformaldehyde and washed three times with PBS. As controls, cells were cultured and fixed in the same fashion on glass control substrates. Raman imaging of cells cultured on cover glass slips exhibited featureless spectra with low intensity in all cases, while cells grown on SERS substrates exhibited clear spectral signatures (compare red and black trace in Fig. 6). In addition to confirming that SERS enhancement occurs, this also supports sufficient adhesion of the cells close to the substrate, also after fixation, which should allow strong amplification of Raman signals related to the molecules in the cellular membrane and the cellular interior (see discussion below).

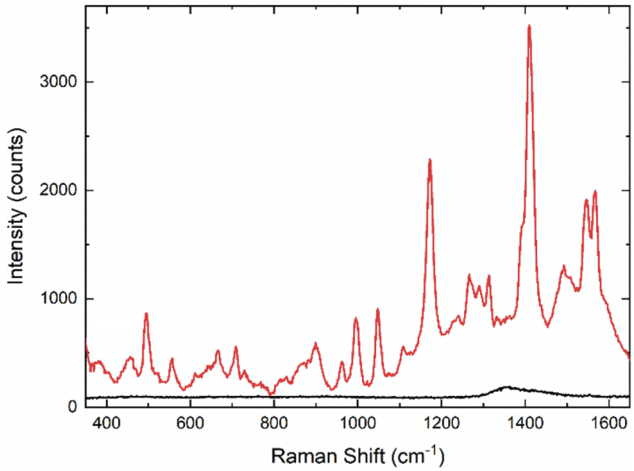

Fig. 6. Representative Raman spectra obtained on mesenchymal stromal cell (BM-MSC) grown on a SERS substrate described in the text (red line) and on a glass cover slip (black line), respectively. The same excitation and collection conditions were used in both cases (excitation: 785 nm, intensity: 2.0×10^5 W·cm^{-2}, acquisition time: 3 s).

5.2. SERS spectra of mesenchymal stromal cells

On selected parts of BM-MSCs cultured on SERS substrates, Raman maps with over 400 spectra each were collected. Several representative SERS spectra for mesenchymal stromal cells are shown in Fig. 7 and tentative assignments of the representative bands are listed in Table 1. The spectra exhibit a wide diversity within different parts of the cell. However, several bands dominate the spectra, and these can be assigned predominantly to proteins and lipids, possibly from the outer cell membrane. The large number of vibrational features shown in Fig. 7 can supply a significant amount of information for the study of the cell behavior on the SERS substrates.

As examples, the assignments of the most prominent bands are listed in Table 1. Peaks at 1067 cm^{-1} of proline and 1322 cm^{-1} of CH_3CH_2 twisting can be considered as markers of collagen I [50], which is synthesized by cells during extracellular matrix formation, confirming

Biomedical Optics EXPRESS

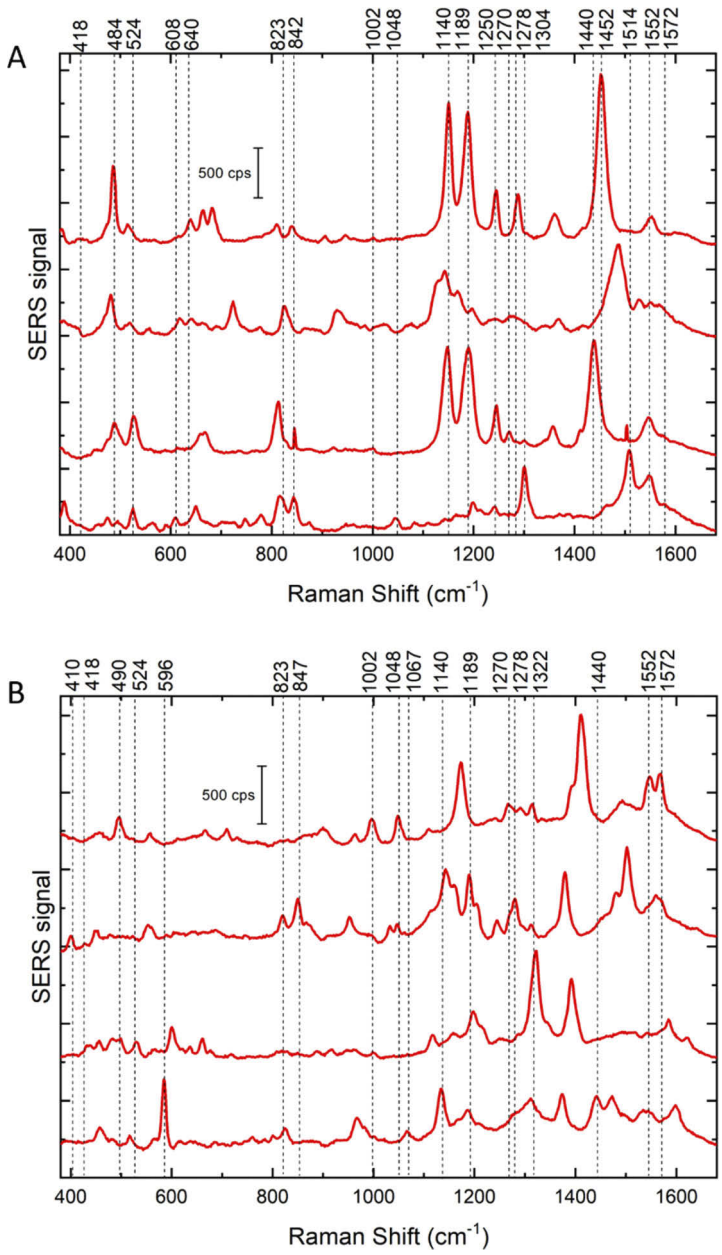

Fig. 7. Representative SERS spectra extracted from the mapping datasets of two different mesenchymal stromal cells on two different SERS substrates (excitation: 785 nm, intensity: 2.0×10^5 W·cm^{-2}, acquisition time: 3 s, step size: 2 µm).

Biomedical Optics EXPRESS

Table 1. Tentative assignments of the most representative bands in the SERS spectra of BM-MSC cells obtained during mapping, based on Refs. [18,50–55,57–59]

Raman shift [cm^{-1}]	Tentative assignments
410	CH_2 bending, phosphatidylinositol
418	CH_2 bending in the ring, cholesterol
484–490	C-O-C ring deformation, carbohydrates, e.g., glycogen
524	S-S disulfide stretching, proteins
596	Phosphatidylinositol
608	Cholesterol
640	C-S stretching and C-S twisting, proteins
823	Ring breathing, tyrosine
842–847	C-O-C skeletal mode, polysaccharides
1002	C-C symmetric stretching, symmetric ring breathing, phenylalanine
1048	Polysaccharide, e.g., glycogen
1067	Proline, e.g., in collagen
1140	C-C stretching, phospholipid alkyl chains
1189	Arginine
1270	C = C groups, unsaturated fatty acids
1278	PO_4^{3-} stretching and amide III, lipids and proteins
1304	CH_2 twist and amide III, lipids and proteins
1322	CH_3CH_2 twisting, collagen
1440	CH_2 deformation, lipids
1514	N-H deformation, proteins
1552	C = C stretching, tryptophan

the origin of the SERS mainly from the cellular exterior and cellular membrane region. However, the most distinctive peaks are those that can be assigned to the vibrations of proteins, e.g., bands at 524 cm^{-1} corresponding to an S-S stretching vibration of disulfide bonds that are found in many different proteins [50,51] or the 1552 cm^{-1} vibration band associated with tryptophan C = C stretching [50]. Other major protein-related vibrations were found at 823 cm^{-1}, 1002 cm^{-1} and 1304 cm^{-1}, representing a ring breathing mode of tyrosine, symmetric stretching of phenylalanine, and a component of the amide III band, respectively [50–54]. The band at 1278 cm^{-1}, assigned to an amide III vibration of proteins, but also to the symmetric stretching of PO_4^{3-} that can be attributed to phosphate groups contained in the phospholipids [50,55,56] has a significant presence in the Raman maps. The lipid-related vibrational modes are represented by bands at 418 cm^{-1} or 608 cm^{-1} of cholesterol, phospholipid alkyl chains at 1140 cm^{-1}, unsaturated fatty acids at 1270 cm^{-1} and CH_2 deformation in lipids at 1440 cm^{-1} [50,52,54,55,57]. Several bands that also often appear in the spectra relate to the vibrations of carbohydrates, such as a peak at 842 cm^{-1} characteristic of polysaccharides [50], known to be major constituents of the extracellular matrix.

5.3. SERS mapping of BM-MSCs

The distribution of some specific vibrational modes recorded for two different cells are shown in chemical images in Fig. 8. The mapped bands can be assigned to proteins, lipids and carbohydrates, which are the main components of the cells, and in the case of the lipid signals possibly to the cell membrane. The maps of bands assigned to cholesterol (418 cm^{-1}), phospholipid alkyl chains (1140 cm^{-1}), polysaccharides (842 cm^{-1}), C = C stretching of tryptophan (1552 cm^{-1}), S-S

Biomedical Optics EXPRESS

disulfide stretching in proteins (524 cm^{-1}), CH_2 deformation in lipids (1440 cm^{-1}), symmetric stretching of phenylalanine (1002 cm^{-1}), and fatty acid (1270 cm^{-1}) show the signal distribution of the respective molecular species. The pixels of high intensity in the maps generated at 1140 cm^{-1} and 1440 cm^{-1} (see Fig. 8, red maps) are co-localized, in agreement with both bands being assigned to lipid chains, mainly phospholipids, known to be the most abundant membrane lipids [60]. Furthermore, the distribution of high signal intensities assigned to phospholipids correlates with the distribution of a high signal of a band at 418 cm^{-1} (see Fig. 8, green map), which indicates the presence of cholesterol, known to co-localize with phospholipids [61]. In Fig. 9, representative spectra from the labeled positions in the map of the band intensity at 418 cm^{-1} of cholesterol are shown, further illustrating the co-localization of the different spectral signals assigned to membrane lipids. In agreement with the above discussion, the spectra from the two labeled positions contain several bands characteristic of lipid vibrations (418 cm^{-1}, 1140 cm^{-1}, 1270 cm^{-1} and 1440 cm^{-1}). The fatty acids in phospholipids can vary in length, hydroxylation, and saturation. As indicative from the signal at 1270 cm^{-1}, unsaturated chains of fatty acids containing *cis*-double bonds are present and co-localize with the high signals from the

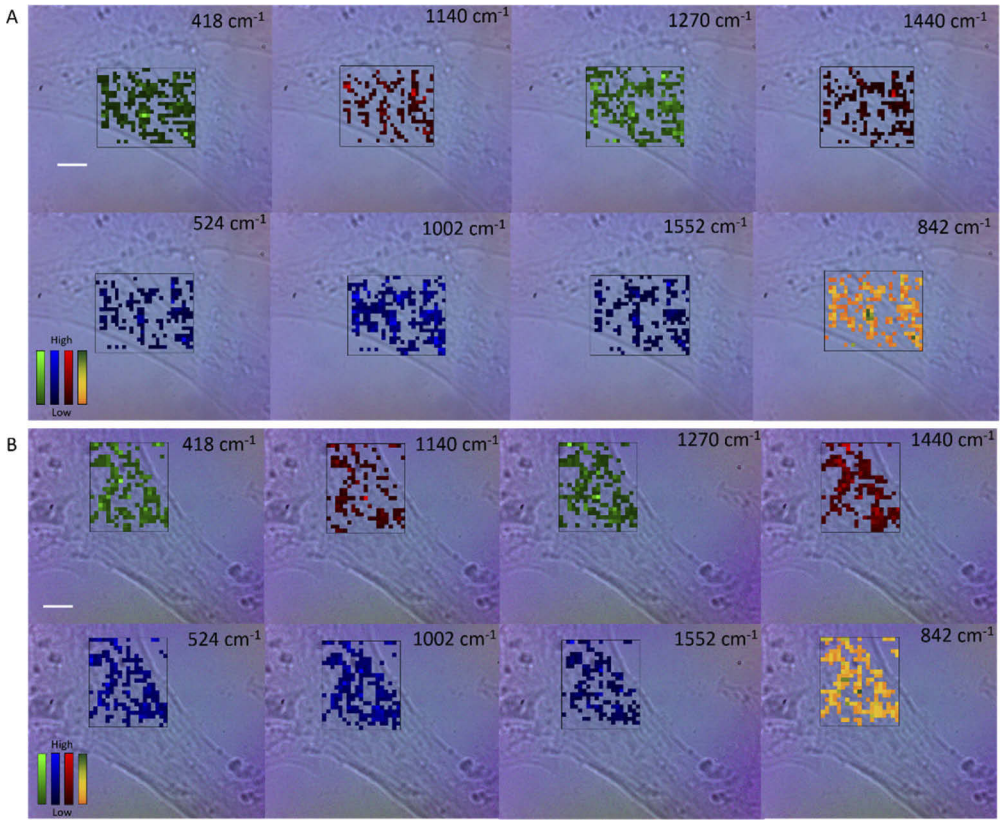

Fig. 8. Raman maps showing the distribution of SERS signals in two different BM-MSCs on two different SERS substrates, and their overlay with microscope images. Raman maps are generated by mapping intensities at 418 cm^{-1} assigned to cholesterol (green), 1140 cm^{-1} to phospholipid alkyl chains (red), 1440 cm^{-1} to CH_2 deformation in lipids (red) and 1270 cm^{-1} to C = C groups in unsaturated fatty acids (green), 524 cm^{-1} to S-S disulfide stretching in proteins (blue), 1002 cm^{-1} to phenylalanine symmetric C-C stretching (blue), 1552 cm^{-1} to tryptophan C = C stretching (blue) and 842 cm^{-1} to polysaccharides (yellow). Scale bars: 10 µm.

Biomedical Optics EXPRESS

phospholipids at 1140 cm^{-1} and 1440 cm^{-1}, confirming this vibrational assignment. Unsaturated fatty acids are known to be responsible for membrane fluidity and adding strength to the cell membrane [61].

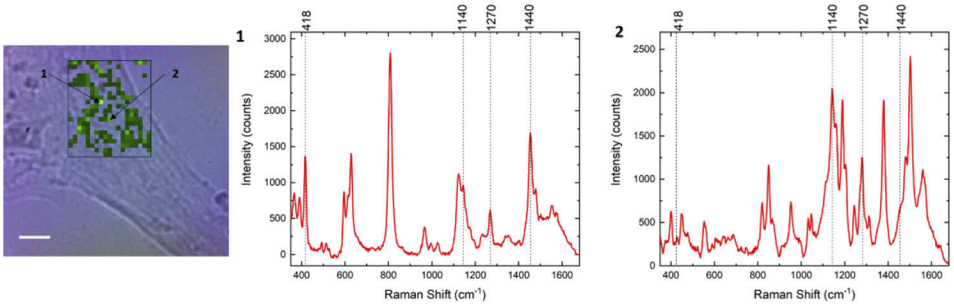

Fig. 9. Chemical image displaying the distribution of the band intensity at 418 cm^{-1}, assigned to cholesterol, followed by example spectra extracted from the maps at two different points labeled in the panel. The SERS spectra represent two different intensities of the 418 cm^{-1} band (excitation: 785 nm, intensity: 2.0×10^5 W·cm^{-2}, acquisition time: 3 s, step size: 2 µm). Scale bar: 10 µm.

Several bands related to protein species were observed in the spectra, including the band at 1002 cm^{-1} of the amino acid phenylalanine and a band at 524 cm^{-1} that can be assigned to the S-S stretching vibration of disulfide bonds. In membrane proteins, such disulfide bonds are formed on the non-cytosolic side [51,62], where they can help stabilize the folded structure of the polypeptide chains. This provides further indication that the SERS substrate mainly probes the outer membrane of the adhering cells. It can be seen in Fig. 8 that the maps at 524 cm^{-1} overlap with the maps of 1002 cm^{-1}, the latter including contributions also from other proteins than exclusively those with an abundance of disulfide bonds. Another characteristic band of proteins can be found at 1552 cm^{-1} and is assigned to the C = C stretching of tryptophan [59]. Its abundance in membrane proteins is also high, and the amino acid preferentially resides near the polar heads of the lipids in the membrane bilayers [63], which also explains the similar distribution to that of the lipids (compare the blue and the red maps in Fig. 8). The map of the band at 842 cm^{-1}, assigned to carbohydrates [50], also often co-localizes with the lipid bands (Fig. 8, yellow maps). This may be due to the fact that the bilayers contain lipids with sugars attached by glycosidic bonds, known as glycolipids, [64] which explains the localization of lipids and carbohydrates at similar positions in the maps.

It can be also noted that the distribution of the intensity of the peak at 1002 cm^{-1}, which is assigned to the ring breathing of phenylalanine [50], widely matches that of the band at 842 cm^{-1}. This would be in agreement with the fact that many outer membrane proteins are glycosylated [65,66].

6. Conclusion

In conclusion, we have employed simple electron-beam evaporation of gold on glass, combined with thermal annealing, to fabricate nm-scale gold nanoisland substrates that provide uniform SERS enhancement across large areas. Both FDTD simulations and experimental results indicate that the origin of improved SERS enhancement relates to the wide distribution of nanoislands sizes and the reduced inter-particle spacing between randomly formed nanoparticles during the deposition and annealing processes. The optimized substrates have demonstrated Raman scattering enhanced by approximately six orders of magnitude which is enough to enable molecular characterization at the single-cell level. The tight adhesion of the mesenchymal

Biomedical Optics EXPRESS

stromal cells to the SERS substrates revealed molecular fingerprints relating to lipids, proteins, and carbohydrates, and their co-localization in chemical maps suggests the probing of cell membrane components. We conclude that this selectivity is a direct effect of the substrate SERS enhancement that results from the direct contact of the cells with the gold substrate. Importantly, it was demonstrated that mesenchymal stromal cells could be cultured directly on the substrates using standard protocols. Although the present work was carried out with fixed cells, we believe that the approach paves the way for using Raman spectroscopy to investigate the behavior of such cells in more detail, including *in vitro* studies of their proliferation and differentiation into different cell lineages. We will report on such measurements in future publications.

Funding

Icelandic Centre for Research (163417-051); Háskóli Íslands; European Research Council (259432 MULTIBIOPHOT).

Acknowledgements

The authors thank Sævar Ingþórsson for assistance with confocal microscopy and Peter Lasch (RKI, Cytospec Inc.) for providing a demo version of CytoSpec software. J.K. acknowledges support from the ERC grant MULTIBIOPHOT.

Disclosures

The authors declare that there are no conflicts of interest related to this article.

References

1. Z. Xu, Z. He, Y. Song, X. Fu, M. Rommel, X. Luo, A. Hartmaier, J. Zhang, and F. Fang, "Topic Review: Application of Raman Spectroscopy Characterization in Micro/Nano-Machining," Micromachines **9**(7), 361 (2018).
2. H. J. Butler, L. Ashton, B. Bird, G. Cinque, K. Curtis, J. Dorney, K. Esmonde-White, N. J. Fullwood, B. Gardner, P. L. Martin-Hirsch, M. J. Walsh, M. R. McAinsh, N. Stone, and F. L. Martin, "Using Raman spectroscopy to characterize biological materials," Nat. Protoc. **11**(4), 664–687 (2016).
3. D. W. Shipp, F. Sinjab, and I. Notingher, "Raman spectroscopy: techniques and applications in the life sciences," Adv. Opt. Photonics **9**(2), 315–428 (2017).
4. J. H. Hibben, "The Raman effect and its chemical applications," Industrial and Engineering Chemistry, News Edition **17**, 556 (1939).
5. M. Fleischmann, P. J. Hendra, and A. J. Mcquillan, "Raman-Spectra of Pyridine Adsorbed at a Silver Electrode," Chem. Phys. Lett. **26**(2), 163–166 (1974).
6. D. L. Jeanmaire and R. P. Van Duyne, "Surface raman spectroelectrochemistry," J. Electroanal. Chem. Interfacial Electrochem. **84**(1), 1–20 (1977).
7. M. G. Albrecht and J. A. Creighton, "Anomalously intense Raman spectra of pyridine at a silver electrode," J. Am. Chem. Soc. **99**(15), 5215–5217 (1977).
8. Q. Jiwei, L. Yudong, Y. Ming, W. Qiang, C. Zongqiang, W. Wudeng, L. Wenqiang, Y. Xuanyi, X. Jingjun, and S. Qian, "Large-area high-performance SERS substrates with deep controllable sub-10-nm gap structure fabricated by depositing Au film on the cicada wing," Nanoscale Res. Lett. **8**(1), 437 (2013).
9. L. Zhang, C. Guan, Y. Wang, and J. Liao, "Highly effective and uniform SERS substrates fabricated by etching multi-layered gold nanoparticle arrays," Nanoscale **8**(11), 5928–5937 (2016).
10. M. Altunbek, G. Kuku, and M. Culha, "Gold Nanoparticles in Single-Cell Analysis for Surface Enhanced Raman Scattering," Molecules **21**(12), 1617 (2016).
11. M. Moskovits and B. Vlckova, "Adsorbate-induced silver nanoparticle aggregation kinetics," J. Phys. Chem. B **109**(31), 14755–14758 (2005).
12. J. Kneipp, H. Kneipp, W. L. Rice, and K. Kneipp, "Optical probes for biological applications based on surface-enhanced Raman scattering from indocyanine green on gold nanoparticles," Anal. Chem. **77**(8), 2381–2385 (2005).
13. J. Kneipp, H. Kneipp, M. McLaughlin, D. Brown, and K. Kneipp, "In vivo molecular probing of cellular compartments with gold nanoparticles and nanoaggregates," Nano Lett. **6**(10), 2225–2231 (2006).
14. A. G. Tkachenko, H. Xie, Y. Liu, D. Coleman, J. Ryan, W. R. Glomm, M. K. Shipton, S. Franzen, and D. L. Feldheim, "Cellular trajectories of peptide-modified gold particle complexes: comparison of nuclear localization signals and peptide transduction domains," Bioconjugate Chem. **15**(3), 482–490 (2004).

Biomedical Optics EXPRESS

15. A. K. Oyelere, P. C. Chen, X. Huang, I. H. El-Sayed, and M. A. El-Sayed, "Peptide-conjugated gold nanorods for nuclear targeting," Bioconjugate Chem. **18**(5), 1490–1497 (2007).
16. F. Lussier, T. Brule, M. Vishwakarma, T. Das, J. P. Spatz, and J. F. Masson, "Dynamic-SERS Optophysiology: A Nanosensor for Monitoring Cell Secretion Events," Nano Lett. **16**(6), 3866–3871 (2016).
17. Y. J. Zhang, Q. Y. Zeng, L. F. Li, M. N. Qi, Q. C. Qi, S. X. Li, and J. F. Xu, "Label-free rapid identification of tumor cells and blood cells with silver film SERS substrate," Opt. Express **26**(25), 33044–33056 (2018).
18. V. Caprettini, J. A. Huang, F. Moia, A. Jacassi, C. A. Gonano, N. Maccaferri, R. Capozza, M. Dipalo, and F. De Angelis, "Enhanced Raman Investigation of Cell Membrane and Intracellular Compounds by 3D Plasmonic Nanoelectrode Arrays," Adv. Sci. **5**(12), 1800560 (2018).
19. D. Wang, W. Zhu, M. D. Best, J. P. Camden, and K. B. Crozier, "Wafer-scale metasurface for total power absorption, local field enhancement and single molecule Raman spectroscopy," Sci. Rep. **3**(1), 2867 (2013).
20. X. Sun and H. Li, "Gold nanoisland arrays by repeated deposition and post-deposition annealing for surface-enhanced Raman spectroscopy," Nanotechnology **24**(35), 355706 (2013).
21. M. Kang, S. G. Park, and K. H. Jeong, "Repeated Solid-state Dewetting of Thin Gold Films for Nanogap-rich Plasmonic Nanoislands," Sci. Rep. **5**(1), 14790 (2015).
22. T. Vo-Dinh, A. Dhawan, S. J. Norton, C. G. Khoury, H. N. Wang, V. Misra, and M. D. Gerhold, "Plasmonic Nanoparticles and Nanowires: Design, Fabrication and Application in Sensing," J. Phys. Chem. C **114**(16), 7480–7488 (2010).
23. X. Cao, Y. Shan, L. Tan, X. Yu, M. Bao, W. Li, and H. Shi, "Hollow Au nanoflower substrates for identification and discrimination of the differentiation of bone marrow mesenchymal stem cells by surface-enhanced Raman spectroscopy," J. Mater. Chem. B **5**(30), 5983–5995 (2017).
24. W. A. El-Said, S. U. Kim, and J.-W. Choi, "Monitoring in vitro neural stem cell differentiation based on surface-enhanced Raman spectroscopy using a gold nanostar array," J. Mater. Chem. C **3**(16), 3848–3859 (2015).
25. S. J. Lee, A. R. Morrill, and M. Moskovits, "Hot spots in silver nanowire bundles for surface-enhanced Raman spectroscopy," J. Am. Chem. Soc. **128**(7), 2200–2201 (2006).
26. C. J. Orendorff, A. Gole, T. K. Sau, and C. J. Murphy, "Surface-enhanced Raman spectroscopy of self-assembled monolayers: sandwich architecture and nanoparticle shape dependence," Anal. Chem. **77**(10), 3261–3266 (2005).
27. Y. Sharma and A. Dhawan, "Plasmonic "nano-fingers on nanowires" as SERS substrates," Opt. Lett. **41**(9), 2085–2088 (2016).
28. A. M. Jubb, Y. Jiao, G. Eres, S. T. Retterer, and B. Gu, "Elevated gold ellipse nanoantenna dimers as sensitive and tunable surface enhanced Raman spectroscopy substrates," Nanoscale **8**(10), 5641–5648 (2016).
29. M. Moskovits, "Persistent misconceptions regarding SERS," Phys. Chem. Chem. Phys. **15**(15), 5301–5311 (2013).
30. M. Sackmann, S. Bom, T. Balster, and A. Materny, "Nanostructured gold surfaces as reproducible substrates for surface-enhanced Raman spectroscopy," J. Raman Spectrosc. **38**(3), 277–282 (2007).
31. M. S. Schmidt, J. Hubner, and A. Boisen, "Large area fabrication of leaning silicon nanopillars for surface enhanced Raman spectroscopy," Adv. Mater. **24**(10), OP11–OP18 (2012).
32. R. La Rocca, G. C. Messina, M. Dipalo, V. Shalabaeva, and F. De Angelis, "Out-of-Plane Plasmonic Antennas for Raman Analysis in Living Cells," Small **11**(36), 4632–4637 (2015).
33. A. Keating, "Mesenchymal stromal cells," Curr. Opin. Hematol. **13**(6), 419–425 (2006).
34. A. I. Caplan, "Mesenchymal stem cells," J. Orthop. Res. **9**(5), 641–650 (1991).
35. T. Squillaro, G. Peluso, and U. Galderisi, "Clinical Trials With Mesenchymal Stem Cells: An Update," Cell Transplant **25**(5), 829–848 (2016).
36. N. Wang, C. Chen, D. Yang, Q. Liao, H. Luo, X. Wang, F. Zhou, X. Yang, J. Yang, C. Zeng, and W. E. Wang, "Mesenchymal stem cells-derived extracellular vesicles, via miR-210, improve infarcted cardiac function by promotion of angiogenesis," Biochim. Biophys. Acta, Mol. Basis Dis. **1863**, 2085–2092 (2017).
37. F. Djouad, P. Plence, C. Bony, P. Tropel, F. Apparailly, J. Sany, D. Noel, and C. Jorgensen, "Immunosuppressive effect of mesenchymal stem cells favors tumor growth in allogeneic animals," Blood **102**(10), 3837–3844 (2003).
38. I. R. Suhito, Y. Han, J. Min, H. Son, and T. H. Kim, "In situ label-free monitoring of human adipose-derived mesenchymal stem cell differentiation into multiple lineages," Biomaterials **154**, 223–233 (2018).
39. X. S. Zheng, I. J. Jahn, K. Weber, D. Cialla-May, and J. Popp, "Label-free SERS in biological and biomedical applications: Recent progress, current challenges and opportunities," Spectrochim. Acta, Part A **197**, 56–77 (2018).
40. N. Lall, C. J. Henley-Smith, M. N. De Canha, C. B. Oosthuizen, and D. Berrington, "Viability Reagent, PrestoBlue, in Comparison with Other Available Reagents, Utilized in Cytotoxicity and Antimicrobial Assays," Int J Microbiol **2013**, 420601 (2013).
41. C. Korzeniewski and D. M. Callewaert, "An enzyme-release assay for natural cytotoxicity," J. Immunol. Methods **64**(3), 313–320 (1983).
42. A. Kudelski, "Raman studies of rhodamine 6G and crystal violet sub-monolayers on electrochemically roughened silver substrates: Do dye molecules adsorb preferentially on highly SERS-active sites," Chem. Phys. Lett. **414**(4-6), 271–275 (2005).
43. Y. Bai, L. Yan, J. Wang, L. Su, N. Chen, and Z. Tan, "Highly reproducible and uniform SERS substrates based on Ag nanoparticles with optimized size and gap," Photonics and Nanostructures - Fundamentals and Applications **23**, 58–63 (2017).

Biomedical Optics EXPRESS

44. A. Kossoy, V. Merk, D. Simakov, K. Leosson, S. Kéna-Cohen, and S. A. Maier, "Optical and Structural Properties of Ultra-thin Gold Films," Adv. Opt. Mater. **3**(1), 71–77 (2015).
45. V. Merk, J. Kneipp, and K. Leosson, "Gap Size Reduction and Increased SERS Enhancement in Lithographically Patterned Nanoparticle Arrays by Templated Growth," Adv. Opt. Mater. **1**(4), 313–318 (2013).
46. P. B. Johnson and R. W. Christy, "Optical Constants of the Noble Metals," Phys. Rev. B **6**(12), 4370–4379 (1972).
47. E. C. Le Ru and P. G. Etchegoin, "Quantifying SERS enhancements," MRS Bull. **38**(8), 631–640 (2013).
48. S. Postaci, B. C. Yildiz, A. Bek, and M. E. Tasgin, "Silent enhancement of SERS signal without increasing hot spot intensities," Nanophotonics **7**(10), 1687–1695 (2018).
49. V. Joseph, A. Matschulat, J. Polte, S. Rolf, F. Emmerling, and J. Kneipp, "SERS enhancement of gold nanospheres of defined size," J. Raman Spectrosc. **42**(9), 1736–1742 (2011).
50. Z. Movasaghi, S. Rehman, and I. U. Rehman, "Raman Spectroscopy of Biological Tissues," Appl. Spectrosc. Rev. **42**(5), 493–541 (2007).
51. A. Rygula, K. Majzner, K. M. Marzec, A. Kaczor, M. Pilarczyk, and M. Baranska, "Raman spectroscopy of proteins: a review," J. Raman Spectrosc. **44**(8), 1061–1076 (2013).
52. L. Mikoliunaite, R. D. Rodriguez, E. Sheremet, V. Kolchuzhin, J. Mehner, A. Ramanavicius, and D. R. Zahn, "The substrate matters in the Raman spectroscopy analysis of cells," Sci. Rep. **5**(1), 13150 (2015).
53. J. Kneipp, H. Kneipp, B. Wittig, and K. Kneipp, "Novel optical nanosensors for probing and imaging live cells," Nanomedicine **6**(2), 214–226 (2010).
54. B. Kann, H. L. Offerhaus, M. Windbergs, and C. Otto, "Raman microscopy for cellular investigations - From single cell imaging to drug carrier uptake visualization," Adv. Drug Delivery Rev. **89**, 71–90 (2015).
55. K. Czamara, K. Majzner, M. Z. Pacia, K. Kochan, A. Kaczor, and M. Baranska, "Raman spectroscopy of lipids: a review," J. Raman Spectrosc. **46**(1), 4–20 (2015).
56. V. Zivanovic, G. Semini, M. Laue, D. Drescher, T. Aebischer, and J. Kneipp, "Chemical Mapping of Leishmania Infection in Live Cells by SERS Microscopy," Anal. Chem. **90**(13), 8154–8161 (2018).
57. D. Borchman, D. Tang, and M. C. Yappert, "Lipid composition, membrane structure relationships in lens and muscle sarcoplasmic reticulum membranes," Biospectroscopy **5**(3), 151–167 (1999).
58. C. Krafft, L. Neudert, T. Simat, and R. Salzer, "Near infrared Raman spectra of human brain lipids," Spectrochim. Acta, Part A **61**(7), 1529–1535 (2005).
59. C. Lee, R. P. Carney, S. Hazari, Z. J. Smith, A. Knudson, C. S. Robertson, K. S. Lam, and S. Wachsmann-Hogiu, "3D plasmonic nanobowl platform for the study of exosomes in solution," Nanoscale **7**(20), 9290–9297 (2015).
60. E. Sezgin, I. Levental, S. Mayor, and C. Eggeling, "The mystery of membrane organization: composition, regulation and roles of lipid rafts," Nat. Rev. Mol. Cell Biol. **18**(6), 361–374 (2017).
61. K. Simons, "Cell membranes: A subjective perspective," Biochim. Biophys. Acta, Biomembr. **1858**(10), 2569–2572 (2016).
62. N. Ruiz, S. S. Chng, A. Hiniker, D. Kahne, and T. J. Silhavy, "Nonconsecutive disulfide bond formation in an essential integral outer membrane protein," Proc. Natl. Acad. Sci. U. S. A. **107**(27), 12245–12250 (2010).
63. A. J. de Jesus and T. W. Allen, "The role of tryptophan side chains in membrane protein anchoring and hydrophobic mismatch," Biochim. Biophys. Acta, Biomembr. **1828**(2), 864–876 (2013).
64. B. Alberts, J. H. Wilson, and T. Hunt, *Molecular Biology of the Cell*, 5th ed. (Garland Science, 2008), pp. xxxiii, 1601, 1690 p.
65. R. P. Berger, M. Dookwah, R. Steet, and S. Dalton, "Glycosylation and stem cells: Regulatory roles and application of iPSCs in the study of glycosylation-related disorders," BioEssays **38**(12), 1255–1265 (2016).
66. U. Coskun and K. Simons, "Cell membranes: the lipid perspective," Structure **19**(11), 1543–1548 (2011).